This article has been accepted for publication in a future issue of this journal, but has not been fully edited. Content may change prior to final publication.
DOI: 10.17775/CSEEJPES.2025.02770

Virtual Oscillator Control Based Shunt Active Power Filter and Field Test

Chenbo Su, *Member*, *IEEE*, Zhitao Wu, *Student Member*, *IEEE*, Wenchuan Wu, *Fellow*, *IEEE*, Chongru Liu, *Senior Member*, *IEEE*

***Abstract*—To overcome the drawbacks of the PI control-based shunt active power filter (SAPF), this article proposes a Virtual Oscillator Control (VOC) based control strategy for SAPF. This VOC-based SAPF has a promising performance in mitigating the active and reactive power ripples. We also prove the proposed SAPF is asymptotically stable within the rated power range. In addition, the strategy for selecting the appropriate parameters of the VOC to ensure the performance of the SAPF is discussed. The simulation and field experimental results show that the VOC-based SAPF significantly outperforms the PI-based one in all cases.**

***Index Terms*—Shunt active power filter, Harmonic current compensation, Virtual Oscillator Control.**

NOTATION

V_{dc}	DC bus voltage
V_{ai}, V_{bi}, V_{ci}	Primary voltages of the three-phase transformer
V_{Ai}, V_{Bi}, V_{Ci}	Secondary voltages of the three-phase transformer
V_{oAB}, V_{oBC}, V_{oCA}	Output voltages of SAPF
i_e	AC current with harmonics on the power grid
i_c	Compensation currents generated by SAPF
L	Resonant inductance
C	Resonant capacitance
i_s	Nonlinear voltage-dependent current source
α	Nonlinear current source coefficient in VOC
σ	Conductance parameter in VOC
K_v	VOC voltage gain
K_i	VOC current gain
i_L	Virtual oscillator inductor current
v	Terminal voltage of the converter
ω	Angular frequency
ϕ	Instantaneous phase angle of the voltage
ε	Oscillator parameter
β	Damping coefficient of VOC
$\overline{V}$	Average amplitude of the SAPF's port voltage
$\overline{\theta}$	Average phase angle of the SAPF's port voltage
$\overline{P}$	Average active power output of the SAPF
$\overline{Q}$	Average reactive power output of the SAPF
v^*	Reference voltage
$\|\|\bullet\|\|_2$	Euclidean norm
Z_{line}	Output filter impedance of the converter
Z_{osc}	Impedance of the shunt branches of the oscillation circuit
$\overline{P}_{eq}$	Average active power output
$\overline{Q}_{eq}$	Average reactive power output
$\overline{V}_{eq}$	Average voltage amplitude
$\overline{V}_{oc}$	Steady-state open circuit voltage
$\overline{V}_{max}$	Maximum steady-state open circuit voltage
$\overline{V}_{min}$	Minimum steady-state open circuit voltage
$\overline{P}_{rated}$	Rated active power
$\overline{Q}_{rated}$	Rated reactive power
$\overline{\theta}_{eq}$	Average phase offsets
$K\Gamma$	Negative definite
$\widetilde{V}$	Disturbance voltage
$\widetilde{\theta}$	Disturbance phase offsets
ω^*	Nominal angular frequency
$\|\Delta\omega\|_{max}$	Maximum frequency deviation
t_{rise}	Rise time of the transient response
t_{max}^{rise}	Allowable maximum rise time
$\delta_{3:1}$	Third harmonic to fundamental amplitude ratio
E_n	Enable signal
ω_{oc}	Harmonic oscillation frequency
$I_{f,a}$, $I_{f,b}$, $I_{f,c}$	Currents filtered by ANF
$\widetilde{P}$	Active power calculated from the currents
$\widetilde{Q}$	Reactive power calculated from the currents
ζ	Quality factor of ANF
ω_n	Trap frequency

This work was supported by the National Natural Science Foundation of China under Grant U23B6008 and U23B20126.

C. Su and W. Wu (Corresponding author) are with the Department of Electrical Engineering, Tsinghua University, Beijing 100084, China.

Z. Wu and C. Liu are with the Department of Electrical Engineering, North China Electric Power University, Beijing 102206, China.

I. INTRODUCTION

A. Motivation

THE harmonic currents generated by the power electronic converter(PEC) interfaced renewable energy resources(RES) may cause safety problems in the power system [1-2]. In particular, the improperly tuned PECs can potentially generate harmonic currents and voltage distortions. As a result, it may cause protection relay malfunctions or component failures in the power system [3-5].

B. Literature review

Various methods have been proposed to suppress the harmonic currents generated by the PECs interfaced with RES and nonlinear loads. These approaches primarily fall into two categories: the first involves enhancing the RES with an additional active damping controller (ADC), and the second consists of using an independent shunt active power filter (SAPF). In [6], an additional ADC was embedded in a three-phase converter to compress the power harmonics. In [7], an adaptive additional damping control signal was introduced to suppress the harmonic currents and improve the stability of the converter with ADC. The authors of [8] present two ADCs for both the d-axis and q-axis control channels of the DFIG's rotor side and optimize the controller parameters using a particle swarm optimization algorithm. However, these ADCs may cause resonance shift to other frequencies, and their performance may deteriorate significantly when the equilibrium point or related parameters change.

Compared to the ADC, the parallel SAPF has high flexibility and efficiency, making it more popular solution for suppressing the current harmonics generated by RESs [9-10]. The SAPF generally consists of a voltage source converter (VSC) and decoupling inductance connected to the grid. The VSC can control the compensation current injected into the system to correct the distorted current waveform. In some literature, the SAPF is also designed to improve the reliability and stability of weak grid-connected converters [11].

Various control schemes have been proposed in the literature for SAPF. The vector-current controller is one of the most common approaches. A classical PI-based vector-current controller is developed for SAPF in [12]. He *et al*. [13] present a proportional multi-resonant controller for harmonic compensation. Swen Bosch *et al*. [14] combine the PI-based current control with a notch filter to realize the predictive current control. However, the wideband-frequency resonance may occur if the gain value of the PI-based controller is not appropriately tuned, which limits the applicability of the PI-based SAPF [15]. Meanwhile, the use of the phase-locked loop (PLL) may also lead to the risk of sub- or super-synchronization-frequency resonance. To solve these problems, nonlinear controllers are proposed as a promising solution. In [16] and [17], the hysteresis current controller (HCC) is proposed for the hybrid SAPF, which shows fast transient response and good steady-state performance. However, it should be noted that the high switching frequency results in a significant inductance to obtain an acceptable current waveform. As a result, there may be a risk of high-frequency resonance. In addition, some nonlinear control methods are utilized for SAPF to generate the compensation current, such as the super-twisting sliding mode controller produced in [18]. However, the initial operating point will affect the convergence performance and regulation of the super-twisting sliding mode-based SAPF.

Recently, the improved virtual oscillator control (VOC) has been applied to the power electronic inverters in some microgrid and regional power grid scenarios [19-20]. A type of dispatchable VOC (dVOC) has been developed to achieve grid-connected control of PV inverters, as it enables secondary control of active and reactive power [21]. Based on the above literature, it is revealed that VOC presents appealing advantages at both the inverter and system levels. From a system-level perspective, synchronization emerges in networks of VOC-integrated grid-connected inverters without relying on any communication infrastructure, and primary voltage and frequency regulation objectives are fulfilled in a decentralized manner. At the circuit level, each inverter can rapidly stabilize arbitrary initial conditions and load transients to a stable limit cycle. The two characteristics, as mentioned above, endow VOC with the application potential in SAPF and enable it to address specific issues in existing control schemes.

C. Contribution

This paper proposes a new SAPF by adopting the virtual oscillator control (VOC) method to compress the harmonic current. According to our investigation, most SAPFs are modulated by current vector control, and the VOC strategy has not been used in active power filters. This technique can enhance the SAPF by reducing the system voltage ripple and output power ripple and improving the robustness.

To the best knowledge of the authors, the main contributions of our work are as follows:

(1) A novel configuration of the SAPF has been proposed in which three-phase transformers are adopted instead of three independent transformers for each phase. Additionally, each phase circuit comprises six H-bridge units, enabling the generation of seven voltage levels and ensuring excellent compensation current waveforms.

(2) The VOC is first adopted and implemented for the SAPF. We prove that the VOC-based SAPF is asymptotically stable according to our design. Remarkably, this VOC-type SAPF exhibits a circular limit cycle in both steady-state and transient conditions, featuring exceptional output compensation current quality.

(3) Strategies for tuning the parameters of the VOC are proposed to ensure the performance of the SAPF, and the characteristics of the critical parameters associated with the SAPF's transient response are analyzed.

Numerical simulations and field tests justify the advantages of the VOC-based SAPF. Compared to the conventional SAPF, the VOC-based SAPF exhibits significantly improved performance in reducing power ripple and providing voltage support to the system, with a faster response.

The remainder of this paper is organized as follows. Section II presents a new configuration of the SAPF. The proposed VOC-based SAPF and the selection of its main parameters are introduced in section III. Numerical simulations are presented in Section IV, and filed experiments are given in Section V. Finally, conclusions are made in Section VI.

II. DESCRIPTION OF THE SAPF

A typical SAPF consists of a DC power source, a DC side capacitor, a series of DC-AC converters, control circuits, and a coupling inductance connected to the grid. The DC side capacitor serves as an energy storage element. The coupling inductance connected to the grid affects the characteristics of the compensation currents. Fig.1(a) shows the PI-based conventional SAPF, and the output of the DC voltage(+Vdc,0,-Vdc) is fed to the primary of the transformer. The secondary terminals of the transformer are connected in series to generate the phase voltage[22]. It can be seen that the traditional SAPF with cascaded multilevel converters utilizes an independent transformer for each H-bridge IGBT, which increases both the size and cost. Fig.1(b) shows the configuration of our proposed SAPF, which has six H-bridges for each phase and corresponding three-phase transformers. Each phase of the multilevel converter is independent. Then, the voltage across the secondary terminals of the series transformers is connected in a string, resulting in a seven-level output voltage that is supplied to the grid. This configuration is critical to reduce output voltage ripple. The following equations describe the relationship between primary and secondary voltages of the three-phase transformer.

$$\begin{bmatrix} V_{Ai} \\ V_{Bi} \\ V_{Ci} \end{bmatrix} = \begin{bmatrix} 2 & -1 & -1 \\ -1 & 2 & -1 \\ -1 & -1 & 2 \end{bmatrix} \begin{bmatrix} V_{ai} \\ V_{ci} \\ V_{bi} \end{bmatrix} \tag{1}$$

Where the capitalized subscripts *A*, *B*, *C,* represent the secondary side of the transformer, the small letter subscripts *a, b*, *c* indicate the primary side of the transformer, and subscript *i* means the transformer number, as shown in Fig.1(b). The output voltage of SAPF is

$$\begin{bmatrix} V_{oAB} \\ V_{oBC} \\ V_{oCA} \end{bmatrix} = \begin{bmatrix} V_{A1}+V_{A2}+V_{A3} \\ V_{B1}+V_{B2}+V_{B3} \\ V_{C1}+V_{C2}+V_{C3} \end{bmatrix} \tag{2}$$

Moreover, it can be observed from Fig.1(b) that the proposed topological structure of the SAPF applies the common leg operation with a three-phase transformer arrangement, which significantly reduces the number of transformers compared to conventional SAPFs. Such a configuration is quite suitable for a grid-connected system. In addition, the output of the SAPF depends on the accumulated voltages, which are synthesized with corresponding reference currents.

The AC current with harmonics on the power grid can be expressed as:

$$i_e(t) = I_1 \sin(\omega_1 t + \varphi_1) + \sum_{n=0, n\neq 1}^{\infty} I_n \sin(n\omega_n t + \varphi_n) \tag{3}$$

From (3), it can be found that the current can be divided into two parts, the fundamental components $I_1\sin(\omega_1 t+\varphi_1)$ and harmonic components $I_n\sin(n\omega_n t+\varphi_n)$. To compress the harmonics, the compensation currents generated by SAPF i_c should be:

$$i_c(t) = -\sum_{n=0, n\neq 1}^{\infty} I_n \sin(n\omega_n t + \varphi_n) \tag{4}$$

To effectively generate such compensation currents, the control strategy of the SAPF is critical.

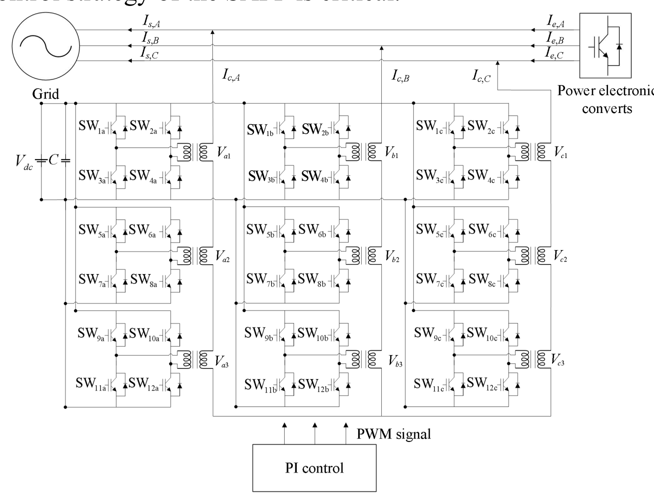

(a). The configuration of the conventional SAPF.

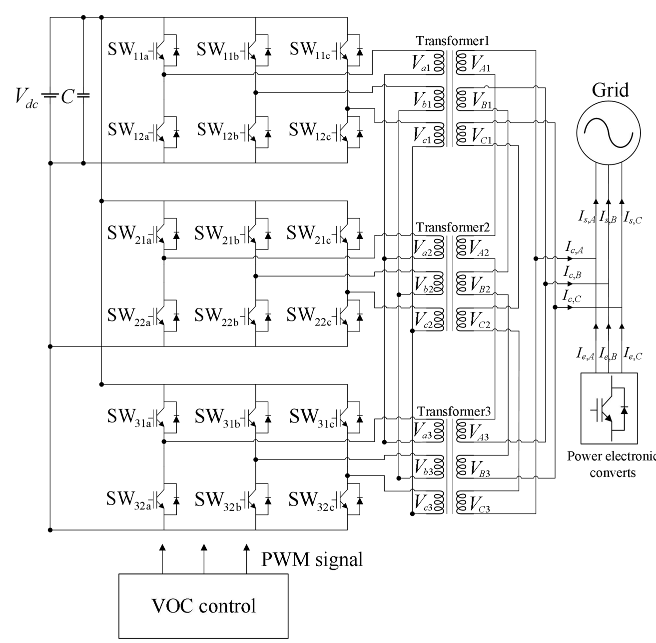

(b). The configuration of the proposed SAPF.

Fig. 1 Different configurations of the conventional and proposed SAPFs

III. CONTROL APPROACHES OF THE VOC-BASED SAPF

In this section, we propose a VOC-based SAPF control strategy to compress the harmonic currents. The virtual oscillator control is based on the Van der Pol oscillation circuit, which mainly consists of three parts: i) Resonant LC circuit: the circuit sets the system frequency and resonant frequency; ii) Nonlinear voltage-dependent current source: $i_s=\alpha v^3$, where α is a positive constant; iii) Negative conductance damping element: $-1/\sigma$. The configuration of VOC is shown in Fig.2.

A. Dynamics of a converter based on VOC

In real practice, optimizing the characteristics of the nonlinear oscillation circuit is a complicated task. To accommodate the performance requirements of various converters, the voltage gain K_v and the circuit gain K_i are given to regulate the output voltage and external circuit levels of the VOC. Figure 2 illustrates that the differential equation of the oscillating circuit can be expressed as follows:

$$\begin{cases} L\dfrac{di_L}{dt}=\dfrac{v}{K_v} \\ C\dfrac{dv}{dt}=-\alpha\dfrac{v^3}{K_v{}^2}+\sigma v-K_v i_L-K_v K_i i \end{cases} \tag{5}$$

Where i_L is the inductance current of the virtual oscillator and v is the terminal voltage of the converter.

$v(t)$ can be expressed as:

$$v(t)=\sqrt{2}V(t)\cos(\omega t+\theta(t))=\sqrt{2}V(t)\cos(\phi(t)) \tag{6}$$

Where ω is the frequency, $\phi(t)$ is the instantaneous phase of the voltage. To simplify the expression, the following variables are introduced [23]:

$$\varepsilon=\sqrt{\frac{L}{C}},\ g(v)=v-\frac{\beta}{3}v^3,\ \beta=\frac{3\alpha}{K_v{}^3\sigma},\tau=\omega^* t=\left(1/\sqrt{LC}\right)t \tag{7}$$

Where ε denotes the square root of the ratio of L and C. β represents the damping coefficient of the Van der Pol oscillator.

Substituting formulas (6) and (7) to (5), we can obtain:

$$\begin{cases} \dot{V}=\dfrac{dV}{d\tau}=\dfrac{\varepsilon}{\sqrt{2}}\left(\sigma g\left(\sqrt{2}V\cos(\phi)\right)-K_v K_i i\right)\cos(\phi) \\ \dot{\phi}=\dfrac{d\phi}{d\tau}=1-\dfrac{\varepsilon}{\sqrt{2}V}\left(\sigma g\left(\sqrt{2}V\cos(\phi)\right)-K_v K_i i\right)\sin(\phi) \end{cases} \tag{8}$$

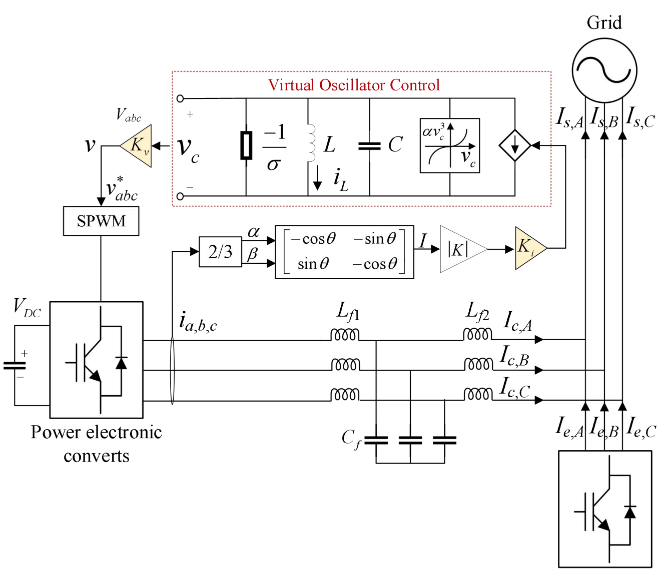

Fig. 2. The control block diagram of the VOC-based SAPF.

The nonlinear differential equations (8) can be simplified and solved by using the averaging method [24], as shown in equation (9), the detailed derivation from equation (8) to (9) is provided in Appendix A.

$$\begin{cases} \dfrac{d}{dt}\overline{V}=\dfrac{\sigma}{2C}\left(\overline{V}-\dfrac{\beta}{2}\overline{V}^3\right)-\dfrac{K_v K_i}{2C\overline{V}}\overline{P} \\ \dfrac{d}{dt}\overline{\theta}=\dfrac{K_v K_i}{2C\overline{V}^2}\overline{Q} \end{cases} \tag{9}$$

Where $\overline{V}$, $\overline{\theta}$, present the average amplitude and phase angle of the SAPF's port voltage. $\overline{P}$ and $\overline{Q}$ are the average active power and reactive power output of the SAPF, respectively.

The system phase trajectory solved by the average model in the quasi-steady state and the phase trajectory of the original nonlinear system are shown in Fig.3, respectively. It is indicated that the error between the average model and the original model is only in the high-order harmonics. This conclusion is also available in the dynamic process [25]. It can be concluded that the differential equations of the above average model can be used to synthesize the virtual oscillator, which provides the ability for the SAPF to regulate the voltage frequency and amplitude.

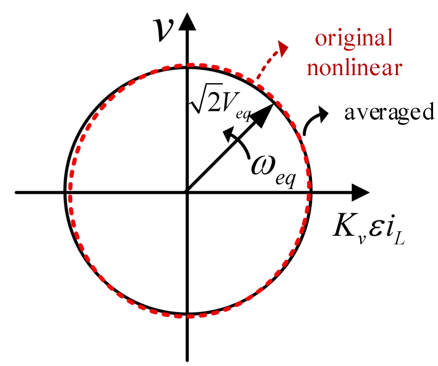

Fig. 3. Superimposed quasi-steady-state limit cycles of the original nonlinear model and the average model.

B. Dynamics of a converter based on VOC

The performance of the VOC is influenced by the parameters set, which include i) current gain K_i and voltage gain K_v, ii) voltage regulation parameters σ and α, and iii) harmonic oscillator parameters L and C.

1) System synchronization conditions

The VOC-based SAPF applies the resonance characteristic of the oscillation circuit to realize synchronization with the grid. It can be observed from Fig.2 that the VOC samples the output currents as input signals for the oscillation circuit to generate the reference voltage v^* abc that matches the frequency of the grid. Moreover, the synchronization ability of the VOC does not depend on the inertia, but depends on the resonance voltage condition. According to the Barbalat lemma, the sufficient condition for the system to have spontaneous synchronization is [26]:

$$\max_{\omega}\left\|\frac{(K_vK_i)^{-1}Z_{line}Z_{osc}}{(K_vK_i)^{-1}Z_{line}+Z_{osc}}\right\|_2\frac{dg(v)}{dv}<1 \tag{10}$$

Where$\|\bullet\|_2$ is Euclidean norm. $Z_{line}=(1/j\omega L_{f1}+1/j\omega L_{f2}+j\omega C_f)^{-1}$ is the output filter impedance of the converter and $Z_{osc}=(1/j\omega L+j\omega C)^{-1}$ is the impedance of the shunt branches of the oscillation circuit.

From (10), it can be seen that the synchronization condition depends on the current gain K_i and voltage gain K_v.

2) Voltage and current gain

Figure 2 shows that the parameters K_v and K_i determine the converter's terminal voltage and output current ratio, respectively. The appropriate value settings of K_v and K_i can be derived from the equilibria of equation (7), it can be expressed as follows:

$$\frac{\sigma}{2C}\left(\overline{V}_{eq}-\frac{\beta}{2}\overline{V}_{eq}{}^{3}\right)-\frac{K_vK_i}{2C\overline{V}_{eq}}\overline{P}_{eq}=0 \tag{11}$$

Where $\overline{P}_{eq}$ and $\overline{V}_{eq}$ are the active power output and average voltage amplitude, respectively. When solving the steady-state open circuit voltage $\overline{V}_{oc}$, the converter power balance condition can be obtained from equation (11)

$$\sigma\beta\overline{V}_{eq}^4-2\sigma\overline{V}_{eq}^2+2K_vK_i\overline{P}_{eq}=0 \tag{12}$$

The positive root of equation (12) is

$$\overline{V}_{eq}=K_v\left(\frac{\sigma\pm\sqrt{\sigma^2-6\alpha(K_i/K_v)\overline{P}_{eq}}}{3\alpha}\right)^{\frac{1}{2}} \tag{13}$$

Equation (13) has two solutions, and the high-voltage solution is locally asymptotically stable within the standardization power flow approximations. It is implicit that the terminal voltage of the VOC is set as the high solution of equation (13) under most operating conditions. The detailed derivation can be found in Appendix B. By substituting P bar, subscript $\overline{P}_{eq}=0$, into equation (13), we can obtain the open-circuit voltage of the inverter.

$$\overline{V}_{\max}=K_v\sqrt{\frac{2\sigma}{3\alpha}} \tag{14}$$

If the capacitor voltage is 1.0 p.u. and the converter terminal voltage is equal to the steady-state open circuit voltage $\overline{V}_{\max}$, we have

$$K_v=\overline{V}_{\max} \tag{15}$$

K_i is selected to match the following situation: when the converter output current is 1.0 (p.u.), the active power is $\overline{P}_{\text{rate}}$. Then, K_i can be set as

$$K_i=\frac{\overline{V}_{\min}}{\overline{P}_{rated}} \tag{16}$$

3) Voltage regulation parameters σ and α

According to the voltage regulation characteristic of equations (14) and (15), the conductance σ and the cubic coefficient of the controlled current source α can be designed. It is worth mentioning that the high-voltage root is a decreasing function of $\overline{P}_{eq}$. Hence, in order to ensure $0\le\overline{P}_{eq}\le\overline{P}_{rate}$, it is necessary to guarantee that the terminal balance voltage of $\overline{V}_{eq}$ is bounded between the limits: $\overline{V}_{\min}\le\overline{V}_{eq}\le\overline{V}_{\max}$.

It can be seen from equation (13) that when $K_v=\overline{V}_{\max}$ is determined, the relationship between σ and α is

$$\alpha=\frac{2\sigma}{3} \tag{17}$$

Then substitute $\overline{P}_{eq}=\overline{P}_{rated}$ and $\overline{V}_{\min}=\overline{V}_{eq}$ into equation (12), it can be derived that.

$$\overline{V}_{\min}=K_v\left(\frac{\sigma+\sqrt{\sigma^2-6\alpha(K_i/K_v)\overline{P}_{rate}}}{3\alpha}\right)^{\frac{1}{2}} \tag{18}$$

Substitute equation (15) and equation (16) into equation (18), and it can be obtained

$$\sigma=\frac{\overline{V}_{\max}}{\overline{V}_{\min}}\frac{\overline{V}_{\max}^2}{\overline{V}_{\max}^2-\overline{V}_{\min}^2} \tag{19}$$

4) Stability analysis of the VOC amplitude and phase dynamics

(1) Amplitude Dynamics analysis

According to the average model discussed above, phase offsets are fixed to their average value, that is, $\overline{\theta}=\overline{\theta}_{eq}$, following which the terminal voltage amplitude dynamics, recovered from (9) can be given as

$$\dot{\overline{V}}_{eq}=\frac{\sigma}{2C}\left(\overline{V}_{eq}-\frac{\beta}{2}\overline{V}_{eq}^3\right)-\frac{K_vK_i}{2C}\left[\overline{i}_{eq}\cos\left(\overline{\theta}_{eq}-\varphi\right)+Z_{osc}\overline{V}_{eq}\right] \tag{20}$$

Theorem 1 *(Local Exponential Stability of Decoupled Amplitude Dynamics):* Consider the decoupled terminal voltage amplitude dynamics in (37). Suppose that each inverter is loaded according to (16). If an equilibrium $\overline{V}_{eq}$ satisfied:

$$\overline{V}_{\min}<\overline{V}_{eq}\le\overline{V}_{\max} \tag{21}$$

then it is locally exponentially stable.

Proof: Suppose the perturbation occurs of the voltage amplitude around the equilibrium point, given that $\overline{V}=\overline{V}_{eq}+\widetilde{V}$, where $\widetilde{V}$ presents the disturbance. According to equation (17), the differential equation for the perturbation component $\widetilde{V}$ can be obtained, that is, $\dot{\widetilde{V}}=K\,\Gamma\,\widetilde{V}$, where $K=K_iK_v$, and the Γ can be expressed as:

$$\Gamma=\frac{\sigma}{2CK}\left(1-\frac{\beta}{2}\overline{V}_{eq}\right)-\frac{1}{4C}Z_{osc} \tag{22}$$

If we ensure

$$\frac{\alpha}{2K}\left(1-\frac{\beta}{2}\overline{V}_{eq}\right)-\frac{1}{4}Z_{osc}<0 \tag{23}$$

then Γ is negative definite. By Sylvester's inertia theorem [22], the inertia (i.e., the triple of positive, negative, and zero eigenvalues) of Γ and $K\Gamma$ are identical since $K_iK_v>0$ and K is positive definite. Consequently, $K\Gamma$ is negative definite, provided (23) is satisfied. The upper bound $\overline{V}_{eq}$ in (12) is the open-circuit voltage $\overline{V}_{\max}$.

(2) Phase dynamics analysis

Assuming that the terminal voltage amplitudes are fixed to the equilibrium values, that is, $V=\overline{V}_{eq}$ and the phase dynamics presented in equation (9) can be written as

$$\frac{d}{dt}\bar{\theta} = \Delta\omega + \frac{K}{2C\bar{V}_{eq}}\bar{i}_{eq}\sin\left(\bar{\theta}-\varphi\right) \tag{24}$$

Theorem 2 *(Local Exponential Stability of Decoupled Phase Dynamics):* Hypothesize that there exists an equilibrium $\bar{\theta}_{eq}$ meet that

$$\left|\bar{\theta}_{\text{eq}} - \varphi\right| > \frac{\pi}{2} \tag{25}$$

Suppose there are local current sources to inject reactive power. In that case, the condition $|\bar{\theta}_{eq} - \varphi > \pi/2|$ is easily satisfied, and the equilibrium value of the phase $\bar{\theta}_{eq}$ is locally exponentially stable. Notably, the electrical power inverters (i.e., PV inverters) are usually equipped with reactive power compensation devices.

Proof: Assuming the disturbance of the phase happens around the equilibrium point, where $\bar{\theta}=\bar{\theta}_{eq}+\tilde{\theta}$, so the differential equation for the perturbation component $\tilde{\theta}$ can be obtained, that is, $\dot{\tilde{\theta}} = K\Theta\bar{V}_{eq}\tilde{\theta}$, the Θ can be expressed as:

$$\Theta = \frac{K}{2C\bar{V}_{eq}}\bar{i}_{eq}\cos\left(\bar{\theta}_{eq}-\varphi\right) \tag{26}$$

If we ensure$|\bar{\theta}_{eq} - \varphi|>\pi/2$, then Θ is negative definite. Consequently, $K\Theta\bar{V}_{eq}$ is negative definite and, therefore, the phase dynamics are locally exponentially stable.

5) The transient response of VOC related to parameters σ, L and C

The harmonic oscillator elements L and C are determined by the frequency regulation characteristics, rise time, and the ratio of the third harmonic to the fundamental frequency. The converter frequency can be obtained from the frequency regulation characteristic of equation (9)

$$\omega_{eq} = \omega^* + \frac{K_v K_i}{2C\bar{V}_{eq}^2}\bar{Q}_{eq} \tag{27}$$

According to the maximum frequency deviation of design input $|\Delta\omega|_{\max}$, substitute K_v and K_i in equations (15) and (16) into (27), the maximum output reactive power under the minimum allowable terminal voltage $\bar{V}_{\min}$, and the lower bound of capacitance C is

$$C \geq \frac{1}{2|\Delta\omega|_{\max}}\frac{\bar{V}_{oc}}{\bar{V}_{\min}}\frac{\left|\bar{Q}_{rate}\right|}{\bar{P}_{rate}} =: C^{\min}_{|\Delta\omega|_{\max}} \tag{28}$$

Where $\bar{Q}_{rate}$ is the maximum average reactive power that the inverter can obtain. If $\bar{P}=0$, the voltage dynamic response is formulated as

$$\frac{d}{dt}\bar{V} = \frac{\sigma}{2C}\left(\bar{V} - \frac{\beta}{2}\bar{V}^3\right) \tag{29}$$

For the integral on both sides of the ordinary differential equation, the upper and lower limits are set as 0.1 $\bar{V}_{\max}$ and 0.9 $\bar{V}_{\max}$, and the rise time can be obtained

$$t_{rise} = \frac{2}{\varepsilon\sigma}\left[\log\bar{V} - \frac{1}{2}\log\left|1-\frac{\beta}{2}\bar{V}^2\right|\right]_{0.1}^{0.9} \approx \frac{6}{\omega^*\varepsilon\sigma} \tag{30}$$

Observing from equation (30), it is deduced that the gain ε significantly affects the system response speed. Combining equations (19) and (28), take the allowable maximum rise time $t_{\max}^{\text{rise}}$ as the design input, and the upper bound of capacitance C is

$$C \leq \frac{t_{\text{rise}}^{\max}}{6}\frac{\bar{V}_{\max}}{\bar{V}_{\min}}\frac{\bar{V}_{\max}^2}{\bar{V}_{oc}^2 - \bar{V}_{\min}^2} = C^{\max}_{t_{\text{rise}}} \tag{31}$$

The ratio of the amplitude between the third harmonic and the fundamental component is denoted as $\delta_{3:1}$, which can be expressed as[27]

$$\delta_{3:1} = \frac{\varepsilon\sigma}{8} \tag{32}$$

Taking the maximum ratio as the design input, the additional lower bound of capacitance C can be obtained by equations (31) and (32)

$$C \geq \left(\frac{1}{8\omega^*\delta_{3:1}^{\max}}\right)\frac{\bar{V}_{\max}}{\bar{V}_{\min}}\frac{\bar{V}_{\max}^2}{\bar{V}_{oc}^2 - \bar{V}_{\min}^2} = C^{\min}_{\delta_{3:1}} \tag{33}$$

Then, the range of capacitance C can be determined by equations (28), (30) and (33). When the above conditions are met, the inductance L can be obtained from $\omega^* = \sqrt{LC}$. Thus, the harmonic oscillator parameters L and C can be determined by

$$L = \frac{1}{C\left(\omega^*\right)^2} \tag{34}$$

C. The voltage reference for VOC based on the ANF

When the system is in a quasi-steady state, the phase angle offset θ related to the system frequency ω is denoted as:

$$\theta = \int\omega\, dt,\ \omega = \omega^* + \frac{K_v K_i}{2C\bar{V}^2}\bar{Q} \tag{35}$$

Where ω^* is the nominal frequency of the grid, while the harmonic oscillation emerges in the system, the dynamical models for amplitude V and frequency ω are restored as:

$$\begin{cases} \dot{\bar{V}} = \dfrac{\sigma}{2C}\left(\bar{V} - \dfrac{\beta}{2}\bar{V}^3\right) - \dfrac{K_v K_i}{2C\bar{V}}\left(\bar{P} - \tilde{P}\right) \\ \omega = \omega^* + E_n\cdot\omega_{oc} + \dfrac{K_v K_i}{2C\bar{V}^2}\left(\bar{Q} - \tilde{Q}\right) \end{cases} \tag{36}$$

Where, E_n is the enable signal whose value is 0 or 1, and ω_{oc} is the harmonic oscillation frequency, which is detected by interpolated discrete Fourier transform (IDFT) [28], and the harmonic oscillation frequency ω_{oc} can be formed by the superposition of multiple resonant frequencies. $\bar{P}$ and $\bar{Q}$ represent the average values of the system's instantaneous power. Moreover, $\tilde{P}$ and $\tilde{Q}$ respectively represent the active power and reactive power calculated from the currents $I_{f,a}$, $I_{f,b}$, and $I_{f,c}$ filtered by adaptive notch filters (ANF), as shown in Fig.4 (a). A set of ANFs can be configured according to the practical operating conditions. This paper uses four ANFs cascaded to address different operating conditions and harmonic coupling phenomena [29].

The transfer function of the ANF can be expressed as follows:

$$G_{notch}\left(s\right) = \frac{s^2 + \omega_n^2}{s^2 + \zeta s + \omega_n^2} \tag{37}$$

Where ζ is the quality factor, and ω_{n} is the trap frequency. Unlike the bandpass filter, the ANF can automatically adjust its parameters according to the actual project requirements [30], which is suitable for the three-phase stationary coordinate frame. Therefore, the fundamental component will be filtered when the sampled signal passes through the ANF. Then, by subtracting the original signal from the former, the harmonic components can be obtained, which will be used for the calculation of the $\widetilde{P}$ and $\widetilde{Q}$. Then, the voltage reference of the VOC can be obtained, as shown in Fig.4 (b).

To embed the ANF in the control system, it should be discretized and digitized. The Tustin transformation with pre-warping gives a better match between the continuous-time and the discretized mode, and the transfer function of the ANF after the Tustin transform is

$$
\begin{aligned}
G_{notch}(z) &= G_{notch}(s)\Big|_{s=k\cdot\frac{z-1}{z+1}} \\
&= \frac{\left(k^2+\omega_n^2\right)-2\left(k^2-\omega_n^2\right)z^{-1}+\left(k^2+\omega_n^2\right)z^{-2}}{\left(k^2+\omega_n^2+k\zeta\right)-2\left(k^2-\omega_n^2\right)z^{-1}+\left(k^2+\omega_n^2-k\zeta\right)z^{-2}}
\end{aligned}
\tag{38}
$$

To simplify the number of coefficients of the transfer function, the above equation can be rearranged as

$$
G(z)=\frac{1}{2}\cdot\frac{\left(1+x_2\right)-2x_1z^{-1}+x_2\left(z^{-2}+1\right)}{1-x_1z^{-1}+x_2z^{-2}} \tag{39}
$$

Where

$$
\begin{cases}
x_1=\dfrac{2\left(k^2-\omega_n^2\right)}{k^2+\omega_n^2+k\zeta} \\
x_2=\dfrac{k^2+\omega_n^2-k\zeta}{k^2+\omega_n^2+k\zeta}
\end{cases},\quad k=\frac{2}{T_s} \tag{40}
$$

The series notch frequency ω_n is also determined according to the harmonic oscillation frequency identified by the interpolated IDFT. Notably, the enable signal is asserted to 1 exclusively when the measured harmonic amplitude surpasses the threshold. This mechanism serves to mitigate spurious activations of the SAPF arising from transient system perturbations or measurement noise. The value of the threshold set in this paper is 3% of the fundamental wave amplitude, which can be adjusted according to local standards.

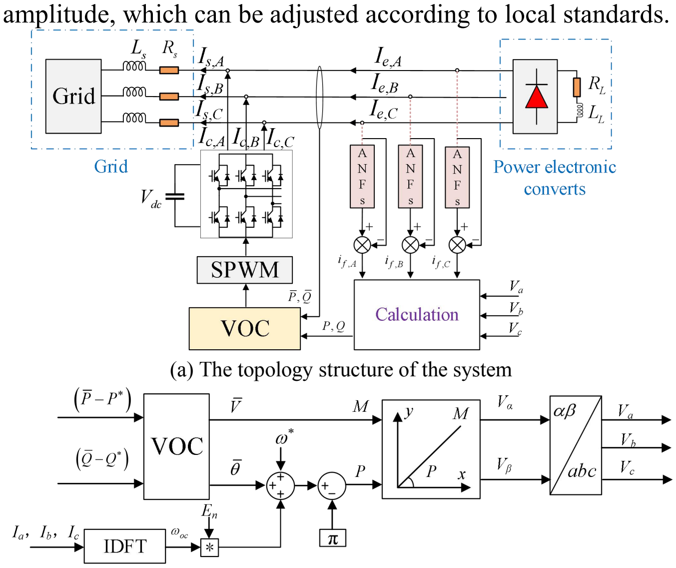

(a) The topology structure of the system

(b) The reference for the VOC

Fig. 4. The reference for the regulation voltage of the SAPF based on VOC

IV. SIMULATION RESULTS

To verify the performance of the proposed SAPF, simulation tests were carried out using PSCAD/EMTDC. The test system topology structure is shown in Fig. 4, in which the power electronic converters are the primary sources of power harmonics. Besides the proposed VOC-based SAPF, the PI-based SAPF [31] and super-twisting sliding mode control-based SAPF have also been implemented and tested for comparison. The parameters of the VOC-based SAPF are listed in Table I.

TABLE I
PARAMETERS OF THE SAPF

Parameters	Values
Line resistance R_L	0.85Ω
Line inductance L_L	1.0mH
Oscillating Circuit inductance L	1.82mH
Oscillating Circuit Capacitor C	980 μF
Rated Voltage $\overline{V}_{eq}$	220V
Rated Active Power $\overline{P}_{rated}$	100MW
DC-bus Capacitor C	1760 μF
DC bus voltage reference V_{dc}	254V
Voltage and Current gain	K_v=1.2, K_i=0.53
Control gains	σ=1.73, α= 1.15

A. The oscillation caused by PLL bandwidth change

The simulation case is set as follows: at 2 seconds, the PLL bandwidth of the power converters increases from 40Hz to 120Hz; after that, the system oscillates. Fig.5(a), Fig.5(b), Fig.5(c), and Fig.5(d) illustrate the different wave shapes of the grid current $\tilde{i}$, in which the proposed method, the PI-based SAPF, active damping, and no filter is adopted, respectively.

In Fig.5(a), since no measures are used to prevent the oscillation, the FFT result (during 2~2.5 seconds) presents that the total harmonic distortion of the current (THD) is approximately 17.5%. Hence, the grid current suffers from significant distortion. The PI-based SAPF is put into the power grid at 2.04 seconds, and the current THD is reduced to 8.5%, as shown in Fig.5(b). However, there is still some distortion in the grid current. Fig. 5(c) shows the simulation results of the super-twisting sliding mode control-based SAPF. Similarly, it was input to the grid at 2.04 seconds, and after approximately 0.1 seconds, it began to take effect, resulting in a decrease in THD to 3.52%. Fig.5(d) presents the compensation results of the proposed VOC-based SAPF. The VOC-based SAPF was activated at 2.04 seconds, and the FFT results show that the harmonics of the grid current are almost entirely eliminated. After 0.04 seconds, the current THD is decreased to 2.6%.

The active power, reactive power, and dc bus voltage with different compensation measures are shown in Fig.6. It can be confirmed that the proposed method suppresses the oscillation very fast and demonstrates the best dynamic performance. Compared to the conventional PI-based SAPF, the proposed method can provide a faster harmonic compensation speed.

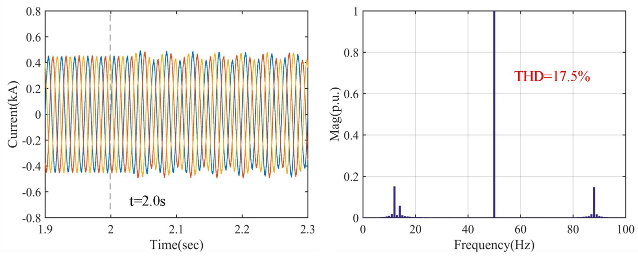

a）without filters

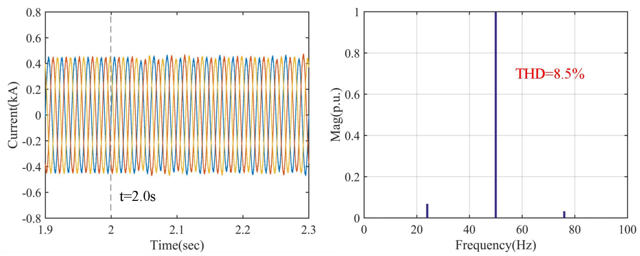

b）with PI-based SAPF

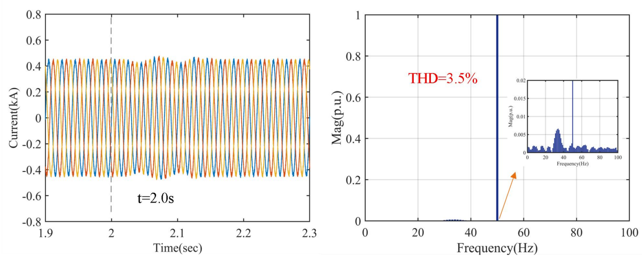

c）with Super-twisting sliding mode control-based SAPF

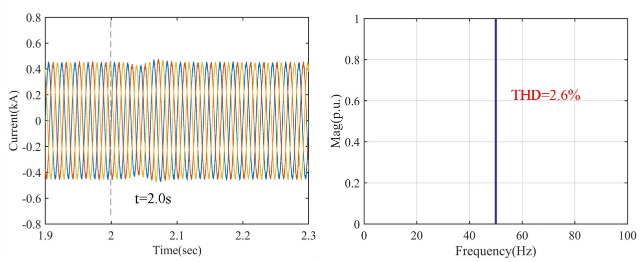

d）with proposed strategy

Fig.5 Current waveform and FFT results of the grid current under different options

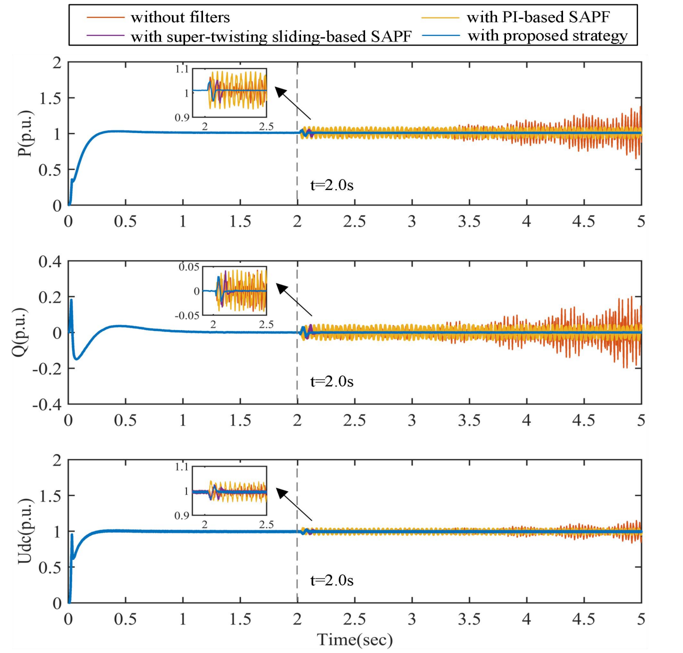

Fig.6 The active power, reactive power, and the dc-link voltage under different compensation methods

B. *The oscillation derived from active power change*

An alternative simulation case is conducted to investigate the suppression effect of the proposed method on oscillations under various operational conditions. Here, the active power reference of the electronic converters is increased to 1.05 (p.u.) after 2 seconds and then returned to 1.0 (p.u.) after 3.75 seconds. The distinct current waveforms are shown in Fig.7 with different compensation approaches.

In Fig.7(a), no suppression strategies are implemented, the grid current is distorted, and the THD increases to 34.7%. Fig.7(b) shows that the PI-based SAPF cannot effectively compensate for the harmonics. From the simulation results of the super-twisting sliding mode control-based SAPF in Fig. 7(c), the THD is reduced to 3.64%. Compared to the other measures, the VOC-based SAPF still exhibits the best performance; the THD of the current decreases to 2.58%, as shown in Fig. 7(d).

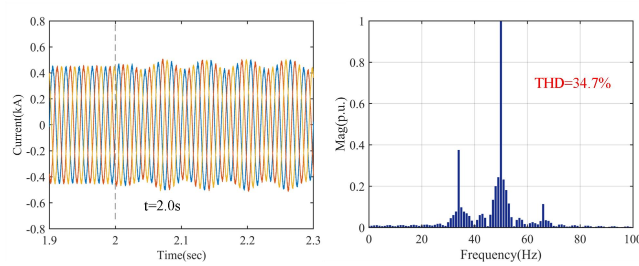

a）without filters

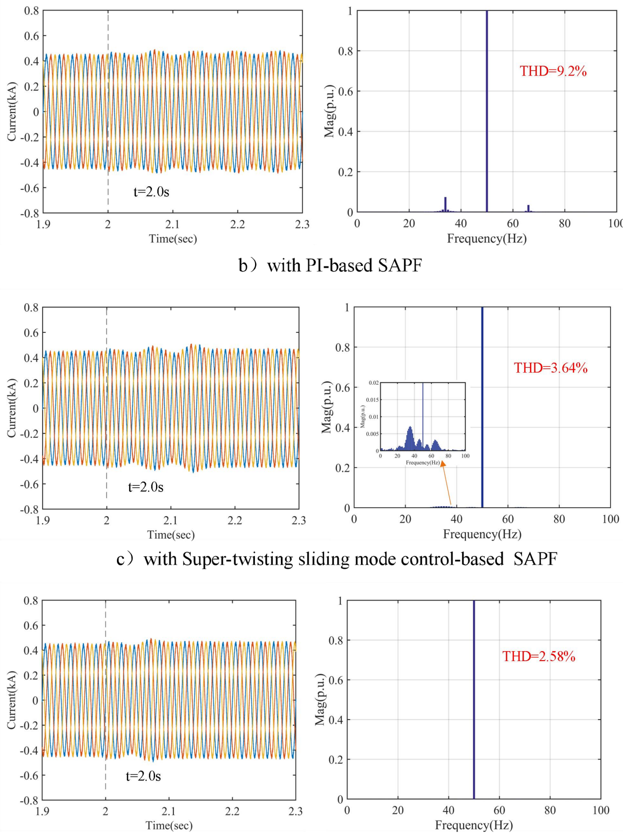

b）with PI-based SAPF

c）with Super-twisting sliding mode control-based SAPF

d）with proposed strategy

Fig. 7 Current waveform and FFT results of the grid current under different compensation methods

In addition, the active power, reactive power, and DC bus voltage with different compensation methods are shown in Fig. 8. Fig. 8 also indicates that the proposed method can eliminate harmonics with the fastest speed.

C. *The Dynamic performance analysis of VOC*

In this subsection, two cases are presented to compare the dynamic performance of the proposed SAPF with that of the PI-based one, particularly in terms of response speed.

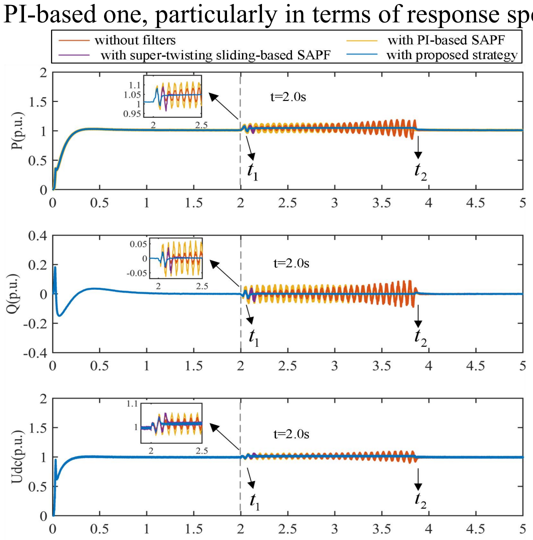

Fig. 8 The active power, reactive power, and the dc-link voltage under different compensation methods

In case one, the harmonic current suppression effect of three different SAPFs is compared under two different oscillation modes. In scenarios 1 and 2, the oscillation is generated by raising the PLL bandwidth. As for scenario 3, the oscillation is produced by increasing the connection impedance between the converters and grids (decreasing the short-circuit ratio (SCR)). Fig. 9 compares the dynamic behavior and response speed of implementing the PI control-based SAPF, the super-twisting sliding mode control-based SAPF, and the VOC-based SAPF in all scenarios, respectively. The horizontal axis represents time, while the vertical axis denotes the error in terms of the quadratic norm between the compensated currents and the reference currents, which is expressed as

$$\left\| i_{ref,k} - i_{c,k} \right\|_2 \quad k = a,b,c \tag{41}$$

From Fig. 9, the VOC-based SAPF can reduce distortion much faster than the super-twisting sliding mode control-based SAPF and PI control-based SAPF in scenarios 1 and 2. In scenario 3, the compensation effect of the VOC-based SAPF is significantly better than that of the other SAPFs in terms of response speed and damping of oscillations. Note that only phase "a" current errors are presented here, but the other two phases have similar results. From this simulation, we can conclude that the VOC-based SAPF has predominant dynamic performance for mitigating system resonance caused by either increasing PLL bandwidths or decreasing power grid strength.

In practice, improper parameter settings of the power converters can lead to harmonic oscillations when operating conditions change. To investigate the dynamic performance of the proposed method, we increase the inner loop control bandwidth of the converters to enhance the output power, and the test results are presented in Fig. 10. It is evident that the VOC-based SAPF reduces harmonics more rapidly. These waveforms also indicate that the VOC-based SAPF outperforms the PI control-based SAPF and super-twisting sliding mode control-based SAPF in suppressing harmonic oscillation.

Therefore, the numerical tests demonstrate that the VOC-based SAPF can more effectively compress harmonics in terms of the time response speed and the final current waveform.

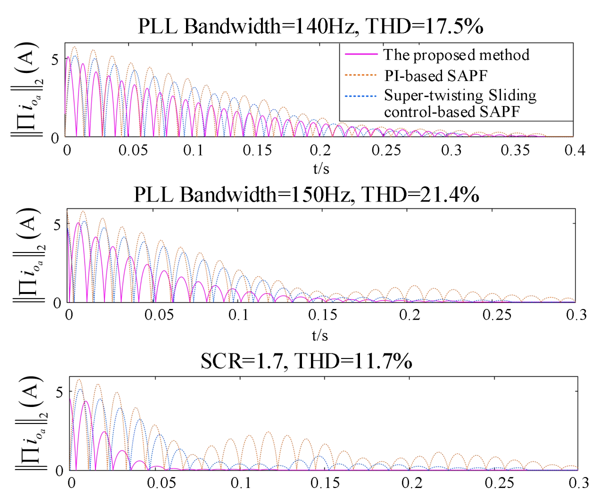

Fig.9 Dynamic performance of different SAPFs for mitigating harmonics incurred by the change of PLL bandwidth and SCR.

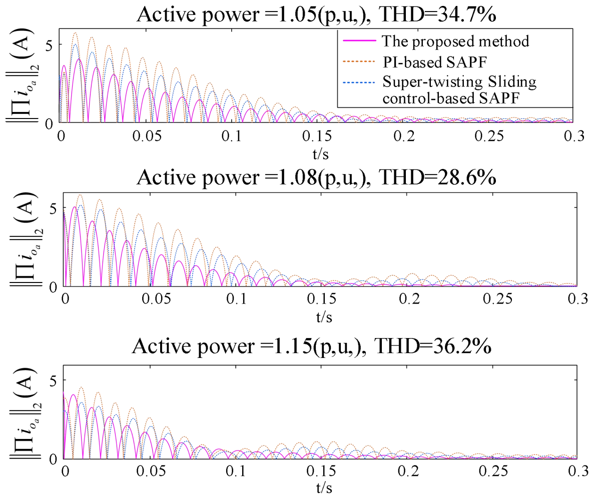

Fig.10 Dynamic performance of different SAPFs for harmonic mitigation at different output power levels of converters.

D. The Impact of critical parameters on the transient response of the VOC-based SAPF

From equation (30), it is evident that the parameter σ dictates the transient response characteristics of the VOC output. A larger σ corresponds to a smaller maximum rise time $t_{\max}^{\text{rise}}$, thereby enhancing the transient response speed of the VOC. However, as the preceding analysis suggests, an excessively large σ leads to a reduction in the dynamic processing of voltage magnitude, thereby deteriorating the system's disturbance rejection capability and stability. Figure 11 presents an analysis of the VOC transient response characteristics under different scenarios with varying σ. As depicted, for a relatively large σ (σ=2.38), the current error demonstrates rapid decay, yet the system exhibits compromised disturbance rejection capability, potentially leading to an increase in current error under certain conditions. Conversely, for a relatively small σ (σ =1.14), the current error decay of the VOC output is sluggish, resulting in suboptimal dynamic performance.

Furthermore, as deduced from Equations (30) and (7), the capacitance C of the oscillatory circuit exerts a significant influence on the transient response characteristics of the VOC output, with a positive correlation established between C and the maximum rise time $t_{\max}^{\text{rise}}$. A larger C is associated with an extended trise max, thereby retarding the transient response speed of the VOC. However, Equation (33) indicates that C cannot be designed below a critical threshold, as this would compromise system stability and induce harmonic distortion in the VOC output. Figure 12 illustrates the VOC output characteristics under different scenarios with parameter C varied. It is revealed that the calculation results of the error current match up with the theoretical analysis.

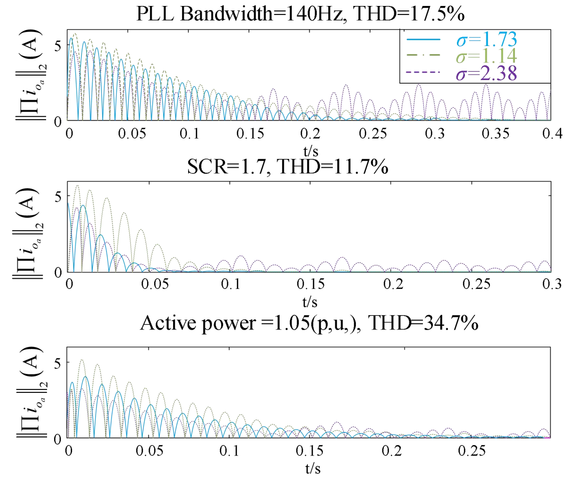

Fig.11 Dynamic performance of SAPFs for various σ.

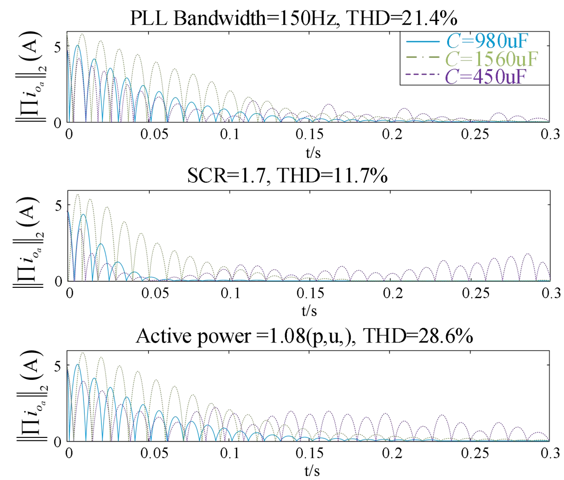

Fig.12 Dynamic performance of SAPFs for various C.

V. FIELD EXPERIMENT

To validate the proposed VOC-based scheme, a SAPF of a 125 kW three-phase LCL-type grid-connected converter controlled by the virtual oscillation method has been implemented in a power supply area of the Shandong province in China, and the connection structure is shown in Fig.13. There are four grid-following PV inverters with a rated power of 125 kW connected to the grid. The power conversion system is used to supply DC power to the SAPF, IGBT switches, and the main inverter components. In addition, the AC side voltage of the PV inverters and the SAPF is 220V, and the high-voltage side of the transformer in the power supply area is 10kV.

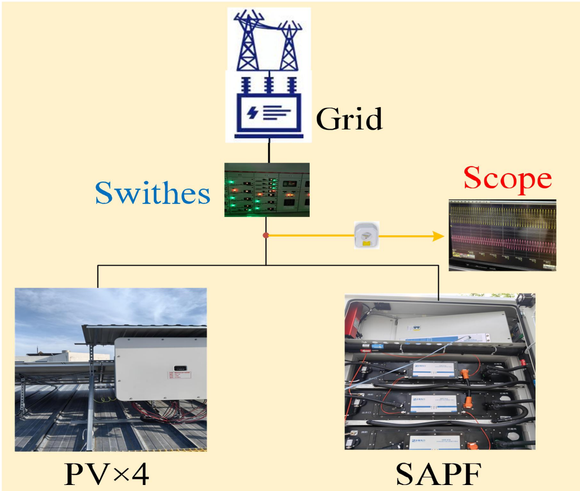

Fig. 13 Wiring diagram of the field experiment.

The experimental test one is as follows: after all four PV inverters are connected to the grid and run stably for 5 seconds, increasing the PLL bandwidth causes the system to oscillate. Then, the SAPF is applied in 1 second. Fig. 14 compares the dynamic experimental waveform of the proposed method with that of the PI-based SAPF. Fig. 14 shows that the grid voltage becomes distorted when the PLL bandwidth is increased. After applying the VOC-based SAPF for 0.22 s, the grid voltage tends to become a sinusoidal wave. However, when the same conditions are set, the super-twisting sliding mode control-based SAPF consumes approximately 0.28 seconds to respond. Meanwhile, the PI-based SAPF takes effect about 0.32 seconds after the filter is applied, while the QPR-based SAPF is slightly faster than the PI-based SAPF. As shown in Fig. 14, the grid current, i_g, is kept in phase with v_g, with a similar transient observed after the SAPF is applied. Additionally, as illustrated by the THD of the system post-harmonic compensation in Fig.14, the VOC-based SAPF proposed in this paper demonstrates optimal compensation performance for the grid current i_g.

Test 2 is carried out as follows: when all four PV inverters are operating in a steady-state condition, the system's load is ramped up, and the PV inverters' output power is increased from 1.0 (p.u.) to 1.08 (p.u.). At the same time, system voltage and current experience waveform distortion. The comparison of the phase-A voltage and current waveforms at the PV inverter output after deploying different types of SAPFs is shown in Figure 15. It is revealed that the SAPF based on the proposed method has the fastest response speed while also demonstrating the best suppression effect. The SAPFs based on PI and QPR control exhibit comparable performance. However, possibly due to the improper setting of control parameters, the sliding mode control-based SAPF performed worse in experiments than in simulations, resulting in a slightly higher system THD after its deployment.

Test 3 procedure: After the system operates stably for 5 seconds, the phase A voltage is short-circuited to ground, reducing the voltage to approximately 66.7% of the rated value. The inverter output current experiences an immediate transient increase, and the SAPF is activated. As shown in Fig.16, all types of SAPFs can provide voltage support. The VOC-based SAPF proposed in this paper takes effect within 0.22 seconds after activation, restoring phase A voltage to approximately 93% of the rated value. PI-based and QPR-based SAPFs exhibit comparable performance, recovering voltage to approximately 85% of the rated value. Notably, the PI-based SAPF suffers from instability after approximately 0.4 seconds of operation, possibly due to PLL issues. The super-twisting sliding mode control-based SAPF raises voltage from 166V to 197V, yet the current THD is somewhat high (6.98%). The test results demonstrate that the proposed method outperforms other SAPF types under voltage disturbances, providing rapid voltage support, suppressing short-circuit currents, and reducing harmonics.

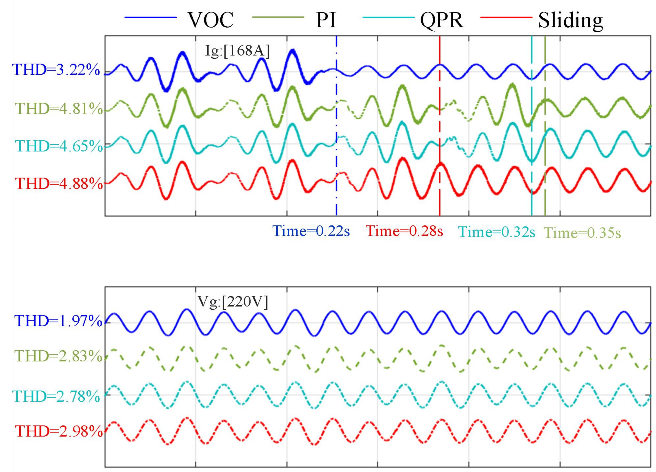

Fig.14 Dynamic experimental waveforms of the grid based on different SAPFs.

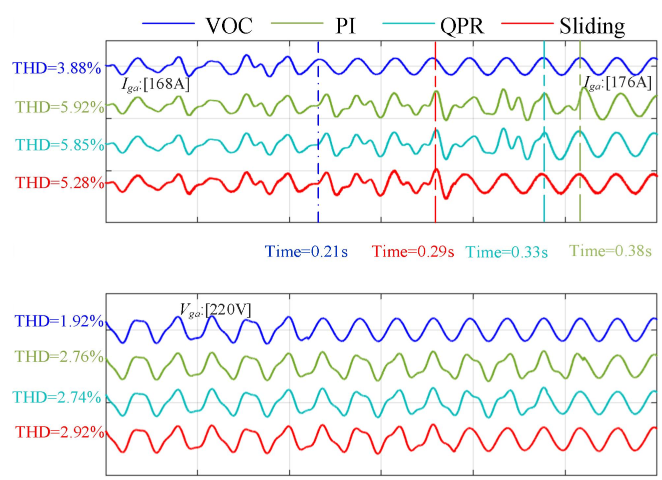

Fig.15 The dynamic responses of different types of SAPFs after experiencing power disturbances.

In summary, the proposed VOC-based SAPF demonstrates superior performance across various experimental scenarios, capable of rapidly providing voltage support, reducing harmonics, and enhancing system stability in response to power and voltage disturbances.

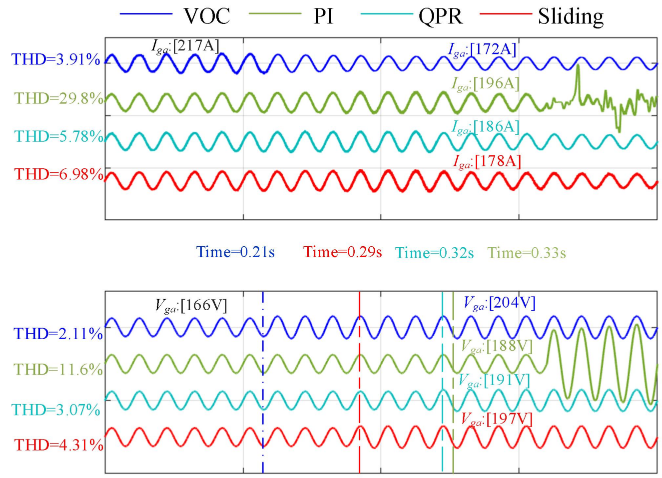

Fig.16 The dynamic responses of different types of SAPFs during a single-phase voltage short-circuit to ground.

VI. CONCLUSION

In this paper, a virtual oscillator control-based synchronous active power filter (SAPF) is proposed to compensate for the unwanted harmonic components of the grid currents. The dynamic performance of the proposed control strategy was evaluated by theoretical analysis. The method for selecting the appropriate parameters to ensure the SAPF's performance is also presented. The simulation and field experiment results demonstrate the satisfactory performance of the proposed method in all cases. In addition, the field tests show that the proposed VOC-based SAPF significantly outperforms other conventional SAPFs in terms of response speed and mitigation of harmonic currents and powers.

APPENDIX A

The instantaneous active-and reactive-power can be expressed as

$$P(t)=v(t)i(t),\quad Q(t)=v\left(t-\frac{\pi}{2}\right)i(t) \tag{A1}$$

The average real and reactive power over an ac cycle of period T are given by

$$\bar{P}=\frac{\omega}{2\pi}\int_{s=0}^{2\pi/\omega}P(s)ds,\quad \bar{Q}=\frac{\omega}{2\pi}\int_{s=0}^{2\pi/\omega}Q(s)ds \tag{A2}$$

From equation (8), the following equation can be obtained

$$\begin{aligned}\dot{V}&=\frac{\varepsilon}{\sqrt{2}}\left(\sigma g\left(\sqrt{2}V\cos(\phi)\right)-K_vK_i i\right)\cos(\phi)\\ \dot{\theta}&=-\frac{\varepsilon}{\sqrt{2}V}\left(\sigma g\left(\sqrt{2}V\cos(\phi)\right)-K_vK_i i\right)\sin(\phi)\end{aligned} \tag{A3}$$

Where $\phi=\tau+\bar{\theta}$. The dynamical systems above are 2π-periodic functions in τ. In the quasi-harmonic limit ε->0, following (A3), we obtain the averaged dynamics:

$$\begin{bmatrix}\dot{\bar{V}}\\ \dot{\bar{\theta}}\end{bmatrix}=\frac{\varepsilon\sigma}{2\pi\sqrt{2}}\int_0^{2\pi}g\left(\sqrt{2}\bar{V}\cos(\phi)\right)\begin{bmatrix}\cos(\phi)\\ \frac{-1}{\bar{V}}\sin(\phi)\end{bmatrix}d\tau-\frac{\varepsilon K_vK_i}{2\pi\sqrt{2}}\int_0^{2\pi}i\begin{bmatrix}\cos(\phi)\\ \frac{-1}{\bar{V}}\sin(\phi)\end{bmatrix}d\tau$$

$$=\frac{\varepsilon\sigma}{2}\begin{bmatrix}\bar{V}-\frac{\beta}{2}\bar{V}^3\\ 0\end{bmatrix}-\frac{\varepsilon K_vK_i}{2\pi\sqrt{2}}\int_0^{2\pi}i\begin{bmatrix}\cos(\phi)\\ \frac{-1}{\bar{V}}\sin(\phi)\end{bmatrix}d\tau \tag{A4}$$

Transitioning (A4) from τ to ωt coordinates and retaining only $O(\varepsilon)$ terms, we get

$$\begin{aligned}\frac{d}{dt}\begin{bmatrix}\bar{V}\\ \bar{\theta}\end{bmatrix}=&\frac{\sigma}{2C}\begin{bmatrix}\bar{V}-\frac{\beta}{2}\bar{V}^3\\ 0\end{bmatrix}-\\ &\frac{K_vK_i\omega}{2\pi\sqrt{2}C}\int_0^{\frac{2\pi}{\omega}}i(t)\begin{bmatrix}\cos(\omega t+\bar{\theta})\\ \frac{-1}{\bar{V}}\sin(\omega t+\bar{\theta})\end{bmatrix}dt\end{aligned} \tag{A5}$$

Recalling the definitions of the instantaneous real and reactive power in (A5), we get

$$\frac{d}{dt}\begin{bmatrix}\bar{V}\\ \bar{\theta}\end{bmatrix}=\frac{\sigma}{2C}\begin{bmatrix}\bar{V}-\frac{\beta}{2}\bar{V}^3\\ 0\end{bmatrix}+\frac{K_vK_i\omega}{4\pi C}\int_0^{\frac{2\pi}{\omega}}\begin{bmatrix}-\frac{P(t)}{\bar{V}}\\ \frac{Q(t)}{\bar{V}^2}\end{bmatrix}dt \tag{A6}$$

Then the equation (9) can be obtained.

APPENDIX B

From a small signal point of view, it can be proved that the high voltage root in (10) is locally asymptotically stable. It is worth noting that the voltage amplitude and phase dependence of the real and reactive power output are described by $\bar{P}_{eq}=p(\bar{V}_{eq},\bar{\theta}_{eq})$ and $\bar{Q}_{eq}=q(\bar{V}_{eq},\bar{\theta}_{eq})$, respectively. By linearizing (11) around the equilibrium point $(\bar{V}_{eq},\bar{\theta}_{eq})$, the linearized system can be obtained.

$$\begin{cases}\partial f_1=\left[\frac{\sigma}{2C}\left(1-\frac{3\beta}{2}\bar{V}_{eq}^2\right)+\frac{K_vK_i}{2C\bar{V}_{eq}^2}\bar{P}_{eq}-\frac{K_vK_i}{2C\bar{V}_{eq}}\frac{\partial\bar{P}_{eq}}{\partial\bar{V}}\right]\Delta\bar{V}-\frac{K_vK_i}{2C\bar{V}_{eq}}\frac{\partial\bar{P}_{eq}}{\partial\bar{\theta}}\Delta\bar{\theta}\\ \partial f_2=\left[-\frac{K_vK_i}{\bar{V}_{eq}^3}+\frac{K_vK_i}{2C\bar{V}_{eq}^2}\frac{\partial\bar{Q}_{eq}}{\partial\bar{V}}\right]\Delta\bar{V}+\frac{K_vK_i}{2C\bar{V}_{eq}^2}\frac{\partial\bar{Q}_{eq}}{\partial\bar{\theta}}\Delta\bar{\theta}\end{cases}$$

(B1)

When the line is inductively loaded, the following is assumed to decouple the linearized amplitude and phase dynamics

$$\frac{\partial\bar{P}_{eq}}{\partial\bar{\theta}}=0 \tag{B2}$$

In order to guarantee the stability of the average amplitude dynamics, we ensure that

$$\frac{\sigma}{2C}\left(1-\frac{3\beta}{2}\bar{V}_{eq}^2\right)+\frac{K_vK_i}{2C\bar{V}_{eq}^2}\bar{P}_{eq}-\frac{K_vK_i}{2C\bar{V}_{eq}}\frac{\partial\bar{P}_{eq}}{\partial\bar{V}}<0 \tag{B3}$$

The stability condition obtained from equation (B3) shows that the stable RMS voltage satisfies

$$\frac{3\sigma\beta}{2}\bar{V}_{eq}^4-\sigma\bar{V}_{eq}^2-K_vK_i\bar{P}_{eq}>0 \tag{B4}$$

For $\bar{P}_{eq}>0$, then $\bar{V}_{eq}$ satisfies

$$\bar{V}_{eq}>K_v\left(\frac{\sigma+\sqrt{\sigma^2+18(K_i/K_v)\alpha\bar{P}_{eq}}}{9\alpha}\right)^{\frac{1}{2}}=\bar{V}_{\lim} \tag{B5}$$

Also, if both roots are made to be real, $\bar{P}_{eq}$ needs to satisfy

$$0 < \overline{P}_{eq} < \overline{P}_{cr} = \frac{\sigma^2}{6\alpha\left(K_i / K_v\right)} \tag{B6}$$

Where $\overline{P}_{\mathrm{cr}}$ is referred to the critical value of the real power. Then, we can bound $\overline{V}_{\mathrm{lim}}$ as follows:

$$\overline{V}_{\mathrm{lim}} < K_v \left(\frac{\sigma + \sqrt{\sigma^2 + 3\sigma^2}}{9\alpha} \right)^{\frac{1}{2}} = K_v \sqrt{\frac{\sigma}{3\alpha}} = \overline{V}_{cr} \tag{B7}$$

From (B7), it follows that $\overline{V}_{\mathrm{eq}}^{\mathrm{high}} > \overline{V}_{\mathrm{lim}}$. Thus, the high voltage solution is locally asymptotically stable.

References

[1] S. Li, H. Wang, Y. Huang, G. He, C. Liu and W. Wang, "Dynamic Interaction and Stability Analysis of Grid-following Converter Integrated Into Weak Grid," in CSEE Journal of Power and Energy Systems, vol. 11, no. 2, pp. 552-566, March 2025.

[2] N. Jiao, S. Wang, J. Ma, T. Liu and D. Zhou, "Sideband Harmonic Suppression Analysis Based on Vector Diagrams for CHB Inverters Under Unbalanced Operation," *IEEE Transactions on Industrial Electronics*, vol. 71, no. 1, pp. 427-437, Jan. 2024,

[3] Y. Zhang, J. Lu and J. Yong, "Harmonic Damping Characteristics of Single-phase Full-bridge Rectifier Based Loads," *CSEE Journal of Power and Energy Systems*, vol. 8, no. 5, pp. 1448-1456, September 2022.

[4] W. Du, Z. Ma, Y. Wang and H. F. Wang, "Harmonic Oscillations in a Grid-Connected PV Generation Farm Caused by an Increased Number of Parallel-Connected PV Generating Units and Damping Controllers," *CSEE Journal of Power and Energy Systems*, vol. 10, no. 6, pp. 2350-2359, November 2024.

[5] G. Lou, S. Li, W. Gu, and Q. Yang, "Distributed Harmonic Power Sharing with Voltage Distortion Suppression in Islanded Microgrids Considering Non-linear Loads," *CSEE Journal of Power and Energy Systems*, vol. 10, no. 1, pp. 117-128, January 2024.

[6] L. Hong, W. Shu, J. Wang and R. Mian, "Harmonic Resonance Investigation of a Multi-Inverter Grid-Connected System Using Resonance Modal Analysis," *IEEE Transactions on Power Delivery*, vol. 34, no. 1, pp. 63-72, Feb. 2019.

[7] A. E. Leon and J. A. Solsona, "Sub-Synchronous Interaction Damping Control for DFIG Wind Turbines," *IEEE Transactions on Power Systems*, vol. 30, no. 1, pp. 419-428, Jan. 2015.

[8] J. Yao, X. Wang, J. Li, R. Liu and H. Zhang, "Sub-Synchronous Resonance Damping Control for Series-Compensated DFIG-Based Wind Farm With Improved Particle Swarm Optimization Algorithm," *IEEE Transactions on Energy Conversion*, vol. 34, no. 2, pp. 849-859, June 2019.

[9] M. -S. Karbasforooshan and M. Monfared, "Adaptive Self-Tuned Current Controller Design for an LCL-Filtered LC-Tuned Single-Phase Shunt Hybrid Active Power Filter," in IEEE Transactions on Power Delivery, vol. 37, no. 4, pp. 2747-2756, Aug. 2022.

[10] X. Du, C. Zhao and J. Xu, "The Use of the Hybrid Active Power Filter in LCC-HVDC Considering the Delay-Dependent Stability," in IEEE Transactions on Power Delivery, vol. 37, no. 1, pp. 664-673, Feb. 2022.

[11] X. Zhang, D. Xia, Z. Fu, G. Wang and D. Xu, "An Improved Feedforward Control Method Considering PLL Dynamics to Improve Weak Grid Stability of Grid-Connected Inverters," *IEEE Transactions on Industry Applications*, vol. 54, no. 5, pp. 5143-5151, Sept.-Oct. 2018.

[12] B. L. G. Costa, V. D. Bacon, S. A. O. da Silva and B. A. Angélico Naik and V. Jammala, "Tuning of a PI-MR Controller Based on Differential Evolution Metaheuristic Applied to the Current Control Loop of a Shunt-APF," *IEEE Transactions on Industrial Electronics*, vol. 64, no. 6, pp. 4751-4761, June 2017.

[13] J. He, B. Liang, Y. W. Li and C. Wang, "Simultaneous Microgrid Voltage and Current Harmonics Compensation Using Coordinated Control of Dual-Interfacing Converters," *IEEE Transactions on Power Electronics*, vol. 32, no. 4, pp. 2647-2660, April 2017

[14] S. Bosch, J. Staiger and H. Steinhart, "Predictive Current Control for an Active Power Filter With LCL-Filter," *IEEE Transactions on Industrial Electronics*, vol. 65, no. 6, pp. 4943-4952, June 2018.

[15] L. Harnefors, M. Hinkkanen, U. Riaz, F. M. M. Rahman and L. Zhang, "Robust Analytic Design of Power-Synchronization Control," *IEEE Transactions on Industrial Electronics*, vol. 66, no. 8, pp. 5810-5819, Aug. 2019.

[16] J. M. S. Callegari, A. L. P. de Oliveira, L. S. Xavier, A. F. Cupertino, D. I. Brandao and H. A. Pereira, "Voltage Detection-Based Selective Harmonic Current Compensation Strategies for Photovoltaic Inverters," *IEEE Transactions on Energy Conversion*, vol. 38, no. 3, pp. 1602-1613, Sept. 2023

[17] Y. -C. Su, P. -H. Wu and P. -T. Cheng, "Design and Evaluation of a Control Scheme for the Hybrid Cascaded Converter in Grid Applications," *IEEE Transactions on Power Electronics*, vol. 35, no. 3, pp. 3139-3147, March 2020

[18] S. Ouchen, M. Benbouzid, F. Blaabjerg, A. Betka and H. Steinhart, "Direct Power Control of Shunt Active Power Filter Using Space Vector Modulation Based on Supertwisting Sliding Mode Control," in IEEE Journal of Emerging and Selected Topics in Power Electronics, vol. 9, no. 3, pp. 3243-3253, June 2021.

[19] Y. Peng, Z. Shuai, L. Che, M. Lyu and Z. J. Shen, "Dynamic Stability Improvement and Accurate Power Regulation of Single-Phase Virtual Oscillator Based Microgrids," *IEEE Transactions on Sustainable Energy*, vol. 13, no. 1, pp. 277-289, Jan. 2022.

[20] V. Gurugubelli, A. Ghosh and A. K. Panda, "Design and Implementation of Optimized Andronov-Hopf Oscillator Control Method for Parallel Inverters in Standalone Microgrid," *IEEE Transactions on Industry Applications*, vol. 59, no. 6, pp. 7013-7026, Nov.-Dec. 2023.

[21] Z. Guo and W. Wu, "Matching Synchronous Machine Control for Improving Active Support of Grid-Forming PV Systems with Enhanced DC Voltage Dynamics," in Journal of Modern Power Systems and Clean Energy, vol. 13, no. 1, pp. 179-189, January 2025.

[22] A. H. Nayfeh, *Introduction to Perturbation Techniques*. Hoboken, NJ,USA: Wiley, 2011.

[23] Z. Shi, J. Li, H. I. Nurdin and J. E. Fletcher, "Comparison of Virtual Oscillator and Droop Controlled Islanded Three-Phase Microgrids," *IEEE Transactions on Energy Conversion*, vol. 34, no. 4, pp. 1769-1780, Dec. 2019.

[24] Z. Wu, Y. Xia and X. Xie, "Stochastic Barbalat's Lemma and Its Applications," *IEEE Transactions on Automatic Control*, vol. 57, no. 6, pp. 1537-1543, June 2012

[25] B. B. Johnson, S. V. Dhople, J. L. Cale, A. O. Hamadeh and P. T. Krein, "Oscillator-Based Inverter Control for Islanded Three-Phase Microgrids," in IEEE Journal of Photovoltaics, vol. 4, no. 1, pp. 387-395, Jan. 2014.

[26] D. Carlson and H. Schneider, "Inertia theorems for matrices: The semidefinite case," *J. Math. Anal. Appl.*, vol. 6, pp. 430–446, 1963.

[27] B. B. Johnson, M. Sinha, N. G. Ainsworth, F. Dörfler and S. V. Dhople, "Synthesizing Virtual Oscillators to Control Islanded Inverters," *IEEE Transactions on Power Electronics*, vol. 31, no. 8, pp. 6002-6015, Aug. 2016.

[28] X. Yang, J. Zhang, X. Xie, X. Xiao, B. Gao and Y. Wang, "Interpolated DFT-Based Identification of Sub-Synchronous Oscillation Parameters Using Synchrophasor Data," in IEEE Transactions on Smart Grid, vol. 11, no. 3, pp. 2662-2675, May 2020.

[29] X. Yue, X. Wang and F. Blaabjerg. Review of Small-Signal Modeling Methods Including Frequency-Coupling Dynamics of Power Converters[J]. IEEE Transactions on Power Electronics, vol. 34, no. 4, pp. 3313-3328, April, 2019.

[30] S. Somkun, S. Srita, T. Kaewchum, A. Pannawan, C. Saeseiw and P. Pachanapan, "Adaptive Notch Filters for Bus Voltage Control and Capacitance Degradation Prognostic of Single-Phase Grid-Connected Inverter," *IEEE Transactions on Industrial Electronics*, vol. 70, no. 12, pp. 12190-12200, Dec. 2023.

[31] B. L. G. Costa, V. D. Bacon, S. A. O. da Silva and B. A. Angélico, "Tuning of a PI-MR Controller Based on Differential Evolution Metaheuristic Applied to the Current Control Loop of a Shunt-APF," in IEEE Transactions on Industrial Electronics, vol. 64, no. 6, pp. 4751-4761, June 2017.

Chenbo Su (Member, IEEE) received the B.S. and Ph.D. degrees in electrical engineering from North China Electric Power University, Beijing, China, in 2014 and 2022, respectively. He is currently working as a postdoctoral research fellow at the Tsinghua University, Beijing, China. His research interests include wind turbine systems and their control, flexible direct current transmission systems and their control.

Zhitao Wu (Student Member, IEEE) received the B.S. degree in electrical engineering from Shanxi University, Taiyuan, China, in 2022. He is currently working toward the Ph.D. degree in electrical engineering with North China Electric Power University. His current research interests include power electronics, renewable energy systems, and grid-forming control.

Wenchuan Wu (Fellow, IEEE) received the B.S., M.S., and Ph.D. degrees from the Department of Electrical Engineering, Tsinghua University, Beijing, China. He is currently a Professor with Tsinghua University. His research interests include Energy Management Systems, active distribution system operations and control, machine learning, and its application in energy systems.

Chongru Liu (Senior Member, IEEE) received the B.S. and Ph.D. degrees in electrical engineering from Tsinghua University, Beijing, China, in 2000 and 2006, respectively. She is currently a Professor, Ph.D. Supervisor, and the Dean of the Undergraduate Academic Affairs Office, North China Electric Power University, Beijing, China. Beijing Science and Technology Nova Talent Support Plan was selected in 2009, and the Ministry of Education Excellent Talents Support Plan for the New Century in 2012.